Amplifier and resonator dynamics of a low-Reynolds-number recirculation bubble in a global framework

OLIVIER MARQUET[1], DENIS SIPP[1], JEAN-MARC CHOMAZ[1,2] AND LAURENT JACQUIN[1]

[1]Departement d'Aerodynamique Fondamentale et Experimentale, ONERA, 92190 Meudon, France
[2]Laboratoire d'Hydrodynamique (LadHyx), CNRS - Ecole Polytechnique, 91128 Palaiseau, France

The stability behaviour of a low-Reynolds-number recirculation flow developing in a curved channel is investigated using a global formulation of hydrodynamic stability theory. Both the resonator and amplifier dynamics are investigated. The resonator dynamics, which results from the ability of the flow to self-sustain perturbations, is studied through a modal stability analysis. In agreement with the literature, the flow becomes globally unstable via a three-dimensional stationary mode. The amplifier dynamics, which is characterized by the ability of the flow to exhibit large transient amplifications of initial perturbations, is studied by looking for the two- and three-dimensional initial perturbations that maximize the energy gain over a given time horizon. The optimal initial two-dimensional perturbations have the form of wave packets localized in the upstream part of the recirculation bubble. It is shown that they are first amplified while travelling downstream along the shear layer of the recirculation bubble and then decay when leaving the recirculation bubble. Maximal energy gain is thus achieved for a time horizon approximately corresponding to the propagation of the wave packet along the whole recirculation bubble. The resonator and amplifier dynamics are associated with different types of structures in the flow: three-dimensional steady structures for the resonator dynamics and nearly two-dimensional unsteady structures for the amplifier dynamics. A comparison of the strength of the two dynamics is proposed. The transient energetic growth of the two-dimensional unsteady perturbations is large at moderate time, compared to the very weak exponential growth of the three-dimensional stationary mode. This suggests that, as soon as there is noise in the system, the amplifier dynamics dominates the resonator dynamics, thus explaining the appearance of unsteadiness rather than the emergence of stationary structures in similar experimental flows.

1. Introduction

Separating and reattaching flows, known as recirculation flows, are widely encountered in aerodynamical applications. They may occur on smooth surfaces due to an adverse pressure gradient, as on airfoils at high angles of attack, or they may be caused by a discontinuity in the surface geometry, as in a backward-facing step flow (see Alving & Fernholz 1996, for the distinction). From an engineering point of view, understanding the laminar–turbulent transition process in these flows is of fundamental importance. For instance, the backward-facing step flow has received much attention at low Reynolds number both experimentally (Denham & Patrick

1974; Armaly *et al.* 1983) and numerically (Ghia, Osswald & Ghia 1989; Kaiktsis, Karniadakis & Orszag 1991; Kaiktsis *et al.* 1996; Williams & Baker 1997, for instance). One of the fundamental open questions is to know if this flow, which belongs to the open shear flow type, exhibits a resonator dynamics similar to the self-sustained oscillations observed in bluff body flows, or an amplifier dynamics typical of free shear layers amplifying external sustained perturbations.

The dynamics of flows at low Reynolds number may be studied in the context of linear stability theory. Classically, open shear flows were first studied using the local approach of linear stability theory. The fate of perturbations at each streamwise station is analysed by studying the dynamics of the fictitious parallel flow generated by extending to infinity the streamwise velocity profile that prevails at that streamwise station. The global behaviour of the flow is then deduced from the local stability properties by assuming a slow variation of the flow in the streamwise direction. In a local approach, the resonator dynamics characterized by the occurrence of self-sustained oscillations has been linked to the appearance of an absolutely unstable region, a region where amplified perturbations propagate both up- and down-stream. The amplifier dynamics, characterized as the ability of the flow to strongly respond to forcing or to exhibit large transient amplifications of an initial condition, has been attributed to the presence of convectively unstable regions, i.e. regions where perturbations are amplified but travel only downstream.

However real open shear flows are generally non-parallel and the assumption inherent in the local approach is thus not valid. In recent years the global approach of linear stability theory, for which both the streamwise and normal flow directions are considered as eigendirections, has received much attention thanks to the increase of computational capacities. In such an approach, the resonator dynamics is studied by examining the spectrum of the linearized Navier–Stokes equations. To that end, a global stability analysis is performed assuming perturbations in the form of temporal global modes, i.e. structures growing exponentially in time. If the temporal growth rate of the leading global mode is positive, the base flow is said globally unstable and the flow may exhibit a resonator dynamics. The first global stability analyses were performed in the late 1980s by Zebib (1987) and Jackson (1987) on bluff body flows and have successfully described the appearance of the von Kármán street.

Only a few studies have attempted to describe the amplifier dynamics in a global stability theory approach. It has been recognized that a modal stability analysis fails to capture transient energetic amplifications. However, this amplification may be captured by describing the perturbations as a superposition of global modes (Schmid & Henningson 2002; Ehrenstein & Gallaire 2005; Åkervik *et al.* 2007). Indeed, as a result of the non-normality of the linearized Navier–Stokes operator (Trefethen *et al.* 1993), global modes are non-orthogonal. Their cooperation may thus induce large transient energetic amplifications. Note that the superposition and cooperation of modes has first introduced to explain subcritical transition in parallel shear flows (Butler & Farrell 1992; Schmid 2007, for a review). In the case of boundary layers, Ehrenstein & Gallaire (2005) have shown that the transient energy amplification of a localized wave packet stems from the time-evolution of a finite number of initially excited stable global modes. An alternative method is adopted in the present paper. The flow dynamics is not reduced to the superposition of a small number of global modes, which remains questionable, but rather described by considering the full dynamics. For this, the temporal evolution of the perturbations is described by marching the full linearized Navier–Stokes equations in time. This new approach yields a general formalism to measure the amplifier dynamics of real open shear flows in a spatial global approach.

The global stability analysis of a backward-facing step flow characterized by a step expansion ratio of 2 has recently been performed by Barkley, Gomes & Henderson (2002). They considered both two-dimensional and three-dimensional perturbations and therefore fully described the resonator dynamics. They found that the flow remains globally stable with respect to two-dimensional perturbations up to $Re = 1500$, the Reynolds number being based on the maximum inlet velocity and step height. Moreover, they proved that the first bifurcation was obtained at $Re = 750$ for a stationary three-dimensional global mode. Similar results have been obtained by Theofilis, Hein & Dallmann (2000) and Gallaire, Marquillie & Ehrenstein (2007) for recirculation bubbles appearing in different flow configurations. To our knowledge, only Beaudoin *et al.* (2004) have experimentally observed the appearance of a steady transverse-periodic structure in a backward-facing step flow, in agreement with these global stability results. The relevance of the global stability analysis to describe the flow dynamics observed in experiments or numerical simulations therefore remains an open question.

Kaiktsis *et al.* (1991) have performed two-dimensional direct numerical simulations of a backward-facing step flow of expansion ratio 1.94 and reported the appearance of global flow oscillations at (non-dimensional) frequency of order 0.1 for $Re = 495$, i.e. a subcritical Reynolds number according to Barkley *et al.* (2002). They first attributed these flow oscillations to the existence of self-sustained oscillations of the flow, i.e. to the resonator dynamics. However, in a later paper (Kaiktsis *et al.* 1996), they reinvestigated this flow configuration using better resolved direct numerical simulations and did not find global oscillations, i.e the flow is globally stable. But, by imposing impulsive or sustained excitations at the step edge, they found large spatial amplification of perturbations leading to flow oscillations at a frequency similar to that previously obtained. Therefore they suggested that the low spatial resolution in their earlier simulations induced discretization errors which sustained perturbations, thus explaining the appearance of flow oscillations. Even if such a noise is fictitious in a numerical simulation, the resulting dynamics remains physically relevant since experiments are inherently subject to noise. Therefore, to obtain a complete description of the flow dynamics, it is necessary to investigate both the resonator and amplifier dynamics. The objective of this paper is to identify and compare these two types of dynamics in the case of a recirculation flow at low Reynolds number.

This study is carried out on a particular configuration which consists of a rounded backward-facing step for the lower wall and a curved upper wall. The resulting recirculation bubble on the lower wall is similar to the one studied by Armaly *et al.* (1983), Kaiktsis *et al.* (1996) and Barkley *et al.* (2002), but the design of the upper wall prevents the appearance of any secondary separation for $Re \leqslant 1500$.

The paper is organized as follows. In §2, the optimal initial perturbation formalism is introduced in the framework of the global approach of the linear stability theory. The numerical procedure is also briefly described. In §3 the base flow is described and results of the global stability analysis are presented. In §4 the results are presented for successively the two-dimensional and three-dimensional optimal initial perturbations. The strengths of the amplifier and resonator dynamics of the recirculation bubble are compared in §5. Finally a discussion is given in §6.

2. Description of configuration and problem formulation

The particular flow configuration studied in this paper is the curved channel geometry depicted in figure 1. The expansion ratio is equal to $h_o/h_i = 1.28$ where h_i
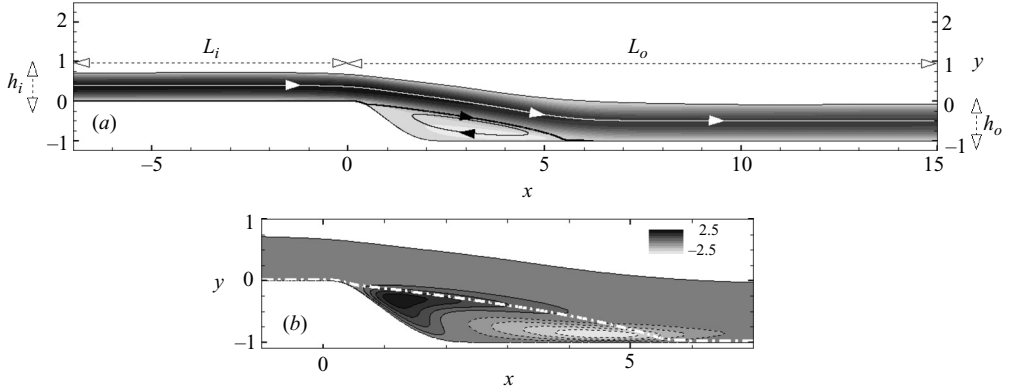
FIGURE 1. (a) Geometry of the curved channel and base flow. The step height is $h = 1$, the channel height $h_i = 0.723$ at the inlet boundary and $h_o = 0.922$ at the outlet boundary so that the expansion ratio is $h_o/h_i = 1.28$. The distances of the inlet and outlet boundaries from the origin of the Cartesian coordinate system (x, y) are respectively $L_i = 7$ and $L_o = 15$. The base flow is depicted by the longitudinal velocity U in the grey levels and by some streamlines. (b) Transverse velocity $\hat{w}$ of the leading three-dimensional eigenmode ($k \sim 2$). The white dash-dotted line depicts the dividing streamline. Parameter setting: $Re = 772$.

and h_o denote the heights of the inlet and outlet sections. The precise definitions of these walls are given in Marquet *et al.* (2007).

The motion of a viscous fluid in this geometry is governed by the homogeneous incompressible Navier–Stokes equations

$$\partial_t \boldsymbol{u} + \nabla \boldsymbol{u} \cdot \boldsymbol{u} = -\nabla p + Re^{-1} \nabla^2 \boldsymbol{u}, \quad \nabla \cdot \boldsymbol{u} = 0, \tag{2.1}$$

where $\boldsymbol{u} = (u, v, w)^{\mathrm{T}}$ stands for the velocity field in a Cartesian coordinate system and p is the pressure. We use the maximum inlet centreline velocity U_∞ and the step height h as reference velocity and length scales, so that the Reynolds number is $Re = U_\infty h / \nu$. We impose a parabolic Poiseuille velocity profile $u = 4y(h_i - y)h_i^{-2}$ at the inlet, no-slip boundary conditions $\boldsymbol{u} = \boldsymbol{0}$ on the solid walls and the outflow boundary condition $p\boldsymbol{n} - Re^{-1}(\nabla \boldsymbol{u}) \cdot \boldsymbol{n} = 0$ at the outlet, where $\boldsymbol{n}$ is the outward unit normal vector.

The velocity and pressure fields are decomposed into a two-dimensional base flow $(\boldsymbol{U}, P) = (U, V, 0, P)$ and a three-dimensional disturbance flow, $\epsilon(\boldsymbol{u}', p') = \epsilon(u', v', w', p')$, where ϵ is the infinitesimal amplitude of the perturbation. The base flow is assumed to be a solution of the steady two-dimensional Navier–Stokes equations

$$\nabla \boldsymbol{U} \cdot \boldsymbol{U} = -\nabla P + Re^{-1} \nabla^2 \boldsymbol{U}, \quad \nabla \cdot \boldsymbol{U} = 0. \tag{2.2}$$

At leading order in ϵ, the perturbation $(\boldsymbol{u}', p')$ is a solution of the Navier–Stokes equations linearized around the base flow $(\boldsymbol{U}, P)$. Since this base flow is homogeneous in the transverse direction z, the three-dimensional perturbation may be decomposed in the form of transverse waves $(\boldsymbol{u}', p')(x, y, z, t) = \{(\tilde{u}, \tilde{v}, \tilde{w}, \tilde{p})(x, y, t) \exp[\mathrm{i}kz] + \mathrm{c.c.}\}/2$ where k is the real transverse wavenumber and c.c. stands for the complex conjugate. Introducing this decomposition into the linearized Navier–Stokes equations shows that a transverse mode $\tilde{\boldsymbol{q}}(x, y, t) = (\tilde{u}, \tilde{v}, \mathrm{i}\tilde{w}, \tilde{p})^{\mathrm{T}}$ associated with the wavenumber k solves the initial value problem,

$$\boldsymbol{B} \cdot \partial_t \tilde{\boldsymbol{q}} = \boldsymbol{A} \cdot \tilde{\boldsymbol{q}}, \quad \tilde{\boldsymbol{q}}(0) = \tilde{\boldsymbol{q}}_0. \tag{2.3}$$

where $\tilde{\boldsymbol{q}}_0$ stands for the initial perturbation. The evolution operator $\boldsymbol{A}$ and the linear operator $\boldsymbol{B}$ are defined by

$$
\boldsymbol{A} = \begin{pmatrix} D - C - \partial_x U & -\partial_y U & 0 & -\partial_x \\ -\partial_x V & D - C - \partial_y V & 0 & -\partial_y \\ 0 & 0 & D - C & k \\ \partial_x & \partial_y & k & 0 \end{pmatrix}, \quad \boldsymbol{B} = \begin{pmatrix} 1 & 0 & 0 & 0 \\ 0 & 1 & 0 & 0 \\ 0 & 0 & 1 & 0 \\ 0 & 0 & 0 & 0 \end{pmatrix} \quad (2.4)
$$

where $D = Re^{-1}\left(\partial_x^2 + \partial_y^2 - k^2\right)$ accounts for the viscous diffusion and $C = U\partial_x + V\partial_y$ for the advection of the perturbation by the base flow. We use homogeneous boundary conditions for $\tilde{u}, \tilde{v}, \tilde{w}$ at the inlet and at the solid walls and the outflow boundary condition $\tilde{p}\boldsymbol{n} - Re^{-1}(\nabla\tilde{u}) \cdot \boldsymbol{n} = 0$ at the outlet. The particular form of operators with the $\tilde{w}$ component in quadrature with the three others allows one to solve an initial value problem (2.3) with real operators $\boldsymbol{A}$ and $\boldsymbol{B}$. The real and imaginary parts of the *a priori* complex vector $\tilde{\boldsymbol{q}}$ are governed by the same evolution equation (2.3), and since $\boldsymbol{A}$ and $\boldsymbol{B}$ are real operators, they evolve independently. Therefore operators can be searched for as a real vector without loss of generality.

We are looking for the initial perturbation that maximizes, at a time T called the time horizon, the energy gain of a perturbation. Let G represent the energy gain over the time period $[0, T]$:

$$
G(\tilde{\boldsymbol{q}}_0) = E(\tilde{\boldsymbol{q}}(T))/E(\tilde{\boldsymbol{q}}_0), \quad (2.5)
$$

where $\tilde{\boldsymbol{q}}(T)$ is given by the resolution on $[0, T]$ of equation (2.3) initialized by $\tilde{\boldsymbol{q}}_0$. The instantaneous energy of the three-dimensional perturbation $\tilde{\boldsymbol{q}}$ is defined using the inner product $(\boldsymbol{a}, \boldsymbol{b}) = \int_\Omega \boldsymbol{a}^T \cdot \boldsymbol{b} \, d\Omega$, and reads $E(\tilde{\boldsymbol{q}}) = (\tilde{\boldsymbol{q}}, \boldsymbol{B} \cdot \tilde{\boldsymbol{q}})/2$. The gain maximized over all possible initial perturbations is called the optimal gain

$$
G_{opt}(k, T) = \max_{\tilde{\boldsymbol{q}}_0} G(\tilde{\boldsymbol{q}}_0), \quad (2.6)
$$

which depends on the transverse wavenumber k and the time horizon T.

To compute the optimal $\tilde{\boldsymbol{q}}_0$, we use an iterative ascent method associated with the evaluation of the gradient of $G(\tilde{\boldsymbol{q}}_0)$. To evaluate this gradient, we use a classical Lagrangian technique to show that (see Corbett & Bottaro 2001)

$$
\nabla G(\tilde{\boldsymbol{q}}_0) = \boldsymbol{B} \cdot \tilde{\boldsymbol{q}}^+(0) - E(\tilde{\boldsymbol{q}}(T))E(\tilde{\boldsymbol{q}}_0)^{-2} \boldsymbol{B} \cdot \tilde{\boldsymbol{q}}_0 \quad (2.7)
$$

where $\tilde{\boldsymbol{q}}^+(0)$ denotes the value at time $t = 0$ of the solution $\tilde{\boldsymbol{q}}^+ = (\tilde{u}^+, \tilde{v}^+, \tilde{w}^+, \tilde{p}^+)$ of the adjoint equations:

$$
\boldsymbol{B} \cdot \partial_t \tilde{\boldsymbol{q}}^+ = \boldsymbol{A}^+ \cdot \tilde{\boldsymbol{q}}^+, \quad \tilde{\boldsymbol{q}}^+(T) = E(\tilde{\boldsymbol{q}}_0)^{-1} \boldsymbol{B} \cdot \tilde{\boldsymbol{q}}(T), \quad (2.8)
$$

The adjoint evolution operator A^+ is defined by

$$
\boldsymbol{A}^+ = \begin{pmatrix} D + C - \partial_x U & -\partial_x V & 0 & -\partial_x \\ -\partial_y U & D + C - \partial_y V & 0 & -\partial_y \\ 0 & 0 & D + C & k \\ \partial_x & \partial_y & k & 0 \end{pmatrix} \quad (2.9)
$$

This adjoint problem is similar to the direct initial value problem (2.3), except that it has to be solved backward in time, starting from the final condition at time $t = T$. Note also that the advection by the base flow has an opposite sign indicating that the adjoint perturbations are convected upstream. We use homogenous Dirichlet boundary conditions for $\tilde{u}^+, \tilde{v}^+, \tilde{w}^+$ at the inlet and on the solid walls. The boundary

condition imposed at the outlet is $\tilde{p}^+ \boldsymbol{n} + Re^{-1}(\nabla \tilde{\boldsymbol{u}}^+) \cdot \boldsymbol{n} = -(U \cdot \boldsymbol{n})\tilde{\boldsymbol{u}}^+$ and results from the definition of the adjoint problem in a spatial continuous framework. The iterative ascent method is based on a steepest ascent algorithm or more efficiently on a generalized version of the conjugate gradient method, also known as the Polak–Ribiere algorithm. In both methods, the optimal ascent step is computed in the following manner. Taking advantage of the linearity of the evolution equations (2.3) the initial perturbation and the associated solution of (2.3) at the iteration $j + 1$ are sought in the form

$$\tilde{\boldsymbol{q}}_0^{j+1} = \tilde{\boldsymbol{q}}_0^j + \alpha^j \nabla G(\tilde{\boldsymbol{q}}_0^j), \quad \tilde{\boldsymbol{q}}^{j+1} = \tilde{\boldsymbol{q}}^j + \alpha^j \tilde{\boldsymbol{q}}_\nabla^j, \qquad (2.10)$$

where α^j is the ascent step and $\tilde{\boldsymbol{q}}_0^{j+1}$, $\tilde{\boldsymbol{q}}_0^j$, $\nabla G(\tilde{\boldsymbol{q}}_0^j)$ are respectively the initial conditions which yield at time T the solutions $\tilde{\boldsymbol{q}}^{j+1}$, $\tilde{\boldsymbol{q}}^j$ and $\tilde{\boldsymbol{q}}_\nabla^j$ through (2.3). The ascent step is chosen so as to maximize the cost function $G(\alpha^j)$ in the direction of the gradient:

$$G(\alpha^j) = \left(a_0 + 2a_1\alpha^j + a_2\alpha^{j^2}\right) \big/ \left(b_0 + 2b_1\alpha^j + b_2\alpha^{j^2}\right)$$

whose coefficients are given by

$$a_0 = (\tilde{\boldsymbol{q}}^j(T), \boldsymbol{B} \cdot \tilde{\boldsymbol{q}}^j(T)), \quad a_1 = (\tilde{\boldsymbol{q}}^j(T), \boldsymbol{B} \cdot \tilde{\boldsymbol{q}}_\nabla^j(T)), \quad a_2 = (\tilde{\boldsymbol{q}}_\nabla^j(T), \boldsymbol{B} \cdot \tilde{\boldsymbol{q}}_\nabla^j(T)),$$
$$b_0 = (\tilde{\boldsymbol{q}}_0^j, \boldsymbol{B} \cdot \tilde{\boldsymbol{q}}_0^j), \quad b_1 = (\tilde{\boldsymbol{q}}_0^j, \boldsymbol{B} \cdot \nabla G(\tilde{\boldsymbol{q}}_0^j)), \quad b_2 = (\nabla G(\tilde{\boldsymbol{q}}_0^j), \boldsymbol{B} \cdot \nabla G(\tilde{\boldsymbol{q}}_0^j)).$$

In practice the algorithm is considered to be converged when the gain G varies by less than 10^{-2}. Typically, a few iterations, usually 6 or 7, are needed to achieve this goal. The main difference between our algorithm and the one used by Corbett & Bottaro (2001) is that these authors, instead of searching for the optimal ascent step, set the gradient to zero which directly gives an evaluation of the initial condition $\tilde{\boldsymbol{q}}_0$ at the next step of the iteration procedure. Comparison between the two approaches shows that, in our computations, the number of iterations is reduced by a factor of two to achieve similar accuracy.

Concerning the numerical procedure, the spatial discretization is carried out through a mixed finite element formulation using P2-P1 Taylor–Hood elements: six-node triangular elements with quadratic interpolation for velocities (P2) and three-node linear triangular elements for the pressure (P1). A Newton iteration method is used to solve the steady Navier–Stokes equations (2.2), starting with an approximate steady solution as a guess. The temporal discretization of the direct (2.3) and adjoint (2.8) linearized Navier–Stokes equations involves a second-order time scheme based on characteristics methods (Boukir *et al.* 1997). The mesh as well as the sparse matrices resulting from the variational formulation of the problems (2.2), (2.3) and (2.8) are generated with the software FreeFem++ (http://www.freefem.org).

3. Description of the base flow and of the resonator dynamics

Figure 1(*a*) represents the longitudinal velocity of the base flow, computed for the Reynolds number $Re = 772$. The flow separates from the lower wall at $x = 0.46$ and reattaches at $x = 5.50$. The dividing streamline, depicted by the bold line in the flow, is the streamline originating from the separation point towards the reattachment point. It defines a closed region where the flow recirculates, called the recirculation bubble. Note that the flow does not separate from the upper wall as long as $Re \leqslant 1500$. This value will define the upper bound of the Reynolds-number parameter study.

The global modes of the present base flow have been described by Marquet *et al.* (2007). The approach consists of assuming an exponential growth in time of
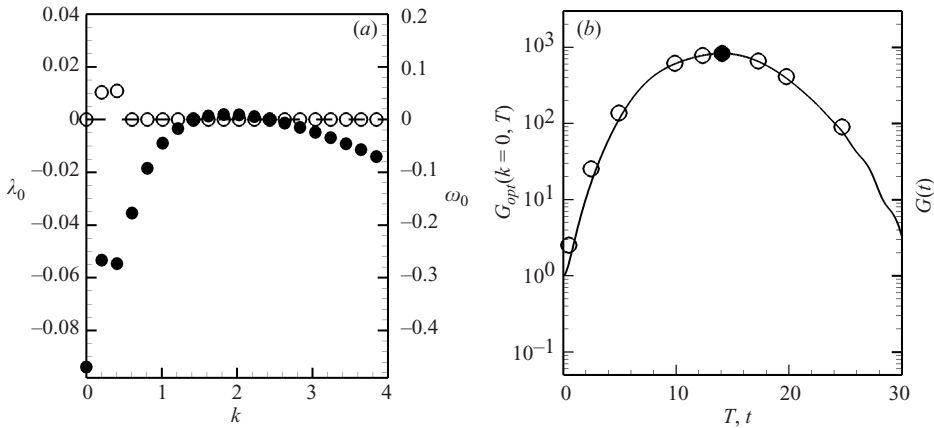
FIGURE 2. (a) Leading eigenvalues $\sigma_0 = \lambda_0 + i\omega_0$ as a function of spanwise wavenumber k. The growth rate λ_0 is depicted by filled circles and the pulsation ω_0 by open circles. (b) Optimal gain of the energy of two-dimensional initial perturbations as a function of the time horizon T. Circles depict the energy of the optimal initial perturbation computed for the corresponding time horizon T. The filled circle indicates the optimal energy gain $G_{opt}(T_{opt})$ corresponding to the optimal time horizon $T = T_{opt}$. The thin solid line shows the effective time-evolution energy of the optimal initial perturbation corresponding to this optimal time horizon T_{opt}. Parameter settings: $Re = 772$.

perturbations, i.e. $\tilde{q} = \hat{q}(x, y) \exp[\sigma t]$. The temporal growth rate λ and pulsation ω of a global mode $\hat{q}(x, y)$ are respectively given by the real and imaginary parts of the complex eigenvalue σ. Figure 2(a) depicts the leading eigenvalue σ_0, i.e. the eigenvalue of largest growth rate, as a function of the transverse wavenumber for the Reynolds number $Re = 772$. The growth rate and pulsation of the leading eigenvalue are depicted in the figure by respectively the filled and open circles. For two-dimensional perturbations ($k = 0$), the growth rate of the leading eigenvalue λ_0 is negative, whereas it is positive for three-dimensional perturbations in the wavenumber range $1.4 < k < 2.4$. The flow is therefore globally stable with respect to two-dimensional perturbations but globally unstable with respect to three-dimensional perturbations. The leading global mode associated with the leading eigenvalue for $k \sim 2$ is non-oscillating ($\omega_0 = 0$). Its transverse velocity, depicted in figure 1(b), shows that the leading global mode is located in the recirculation bubble. This mode is very similar to the three-dimensional leading global mode obtained by Barkley *et al.* (2002) in a flow over a backward-facing step of expansion ratio 2 and by Gallaire *et al.* (2007) in a flow over a bump. It describes the resonator dynamics of the recirculation bubble.

4. Characterization of the amplifier dynamics

The energy gain of two-dimensional perturbations ($k = 0$) is first investigated. Figure 2(b) presents the two-dimensional optimal energy gain $G_{opt}(k = 0, T)$ as a function of the time horizon T (open circles). The optimal energy gain first increases and reaches a maximum value $G_{opt}(k = 0, T = T_{opt}) = 830$ for the time horizon $T_{opt} = 14$, shown in the figure by the filled circle. This time horizon will be called the optimal time horizon in what follows. For larger time horizons the optimal energy gain decreases, becoming less than unity for $T \geqslant 30$. The effective time evolution of the energy gain of the optimal perturbation at $T = T_{opt}$ is plotted in the figure with a solid
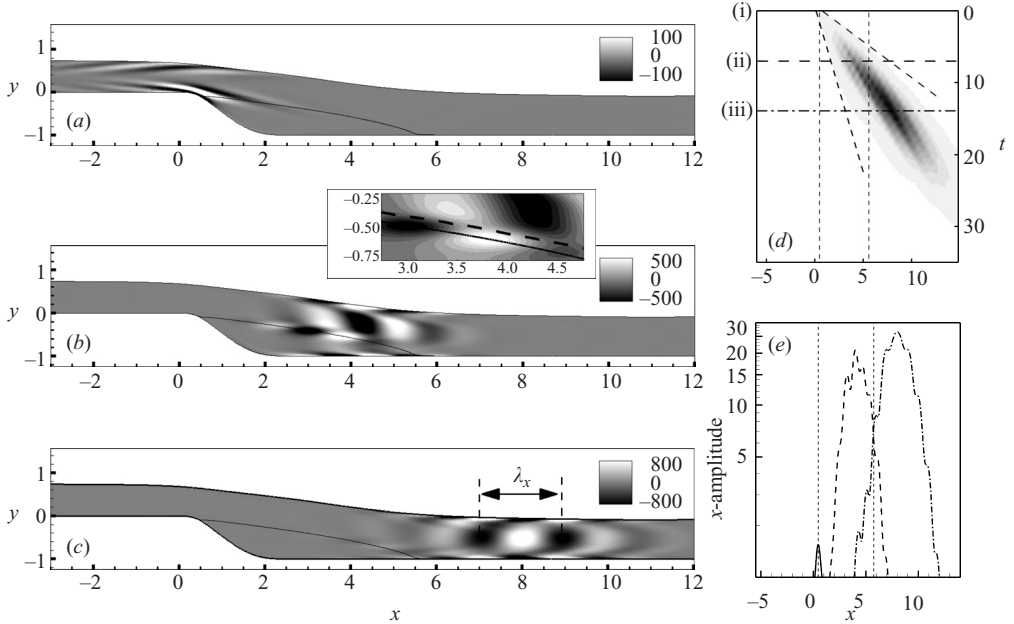
FIGURE 3. Spatio-temporal evolution of the initial perturbation for the optimal time horizon $T = T_{opt}$ whose energy growth is sketched by a solid line in figure 2(b). (a–c) Spatial distribution of the transverse vorticity at different instants of the effective time-evolution (a) $t = 0$, (b) $t = T_{opt}/2$ and (c) $t = T_{opt}$, with a close-up of figure (b). The solid lines in the flow show the dividing streamline and the dashed line in the close-up view of (b) the locus of the inflectional point in the shear-layer profiles. (d) x,t diagram of the x-energy visualized by grey levels (from 1 to 341 by increments of 20). The x-energy is defined at each station x by $\int_{\Gamma(x)} 0.5 \, (u^2 + v^2) \, \mathrm{d}y$ where $\Gamma(x)$ is the corresponding vertical section. The oblique dashed lines show the trailing and leading edges of the wave packet. The horizontal lines show the times 0, $T_{opt}/2$ and T_{opt}. (e) x-amplitude of the wave packet, defined by $\sqrt{\int_{\Gamma(x)} 0.5 \, (u^2 + v^2) \, \mathrm{d}y}$, as a function of x, at times $t = 0$ (solid line), $t = T_{opt}/2$ (dashed line) and $t = T_{opt}$ (dash-dotted line). In (d) and (e), the vertical dashed lines indicate the separation and reattachment locations of the recirculation bubble. Parameter settings: $Re = 772$, $k = 0$.

line. Strikingly, it is nearly optimal for all times, and decays to zero for large times (not shown here) indicating that the flow is globally stable with respect to two-dimensional perturbations.

The spatio-temporal evolution of this optimal initial perturbation is presented in figure 3. The spatial vorticity distribution of the perturbation is plotted in figure 3(a–c) at three times: (a) the initial time $t = 0$, (b) half of the optimal time horizon $t = T_{opt}/2$ and (c) the optimal time horizon T_{opt}. The initial perturbation (figure 3a) takes the form of an elongated wave packet localized in the upstream part of the channel, close to the separation point, and oriented in the opposite direction to the shear of the base flow. For increasing but small time, the wave packet is first advected by the base flow into a more upright orientation (not shown here). This reorientation of the initially tilted wave packet suggests that, at very short times, a mechanism similar to the one described by Orr (1907) contributes to the energetic amplification of the perturbation. For larger times, the wave packet is amplified while travelling downstream along the shear layer of the recirculation bubble (see figure 3b). The wave packet takes the form of vortical structures of opposite sign alternately located

above and below the line of inflection points, which is depicted by the dashed line in the close-up view of figure 3(*b*). This spatial pattern indicates that the energetic amplification of the perturbation is due to the inflectional instability mechanism. While travelling, the vortical structures progressively grow in space. At the optimal time horizon (figure 3*c*), the wave packet is leaving the recirculation bubble. The size of the vortical structures there approximately scales with the outlet channel height h_o and the length of the peak-to-peak amplitude, gives an approximation of the longitudinal wavelength, $\lambda_x \sim 1.85 \sim 2h_o$.

Figure 3(*d*) is a spatio-temporal diagram of the *x*-energy, defined as the energy integrated over the vertical section at each station *x*. Darker grey levels indicate increasing *x*-energy. The positions of the separation ($x = 0.46$) and reattachment points ($x = 5.50$) are given in the figure by the vertical dashed lines, and the horizontal solid, dashed and dash-dotted lines, also denoted (i), (ii) and (iii), indicate the three times 0, $T_{opt}/2$ and T_{opt}. For these times the longitudinal distribution of the *x*-amplitude of the wave packet, defined as the square root of the *x*-energy, is plotted in figure 3(*e*), where the solid line is for $t = 0$, the dashed line for $t = T_{opt}/2$ and the dash-dotted line for $t = T_{opt}$. Initially the energy of the wave packet viewed in figure 3(*a*) is clearly concentrated in the vicinity of the separation point, as seen in figure 3(*e*). For $t \leqslant T_{opt}$ the wave packet is amplified while propagating downstream, as previously noted. During this amplification process, an increase of the spatial extent of the wave packet may be seen in figures 3(*d*) and 3(*e*). This is characterized in figure 3(*d*) by different propagation speeds of the trailing and leading edges, shown by the oblique dashed lines. The trailing edge propagates at low speed $x/t = 0.21$ and the leading edge at high speed $x/t = 0.99$. For larger times ($t \geqslant T_{opt}$) the trailing and leading edges approximately propagate at the same speed $x/t = 0.54$, which reflects the average speed of the flow in the downstream channel, i.e. $2h_o/(3h_i) = 0.52$ (recall that 2/3 is the average speed of the upstream Poiseuille flow). This observation is compatible with the large scales of the perturbations obtained in the downstream channel.

The energy of the wave packet decreases strikingly fast for $T \geqslant 20$ and is of the order of the initial energy when reaching the outlet at $T \sim 30$. This shows that the downstream part of the channel, where the base flow is close to a Poiseuille flow, is responsible for strong attenuations of the perturbation energy. Hence, the perturbation energy is vanishingly small when it reaches the outlet boundary. Therefore, the position of the outlet has no impact on the present results (note that this has been checked directly by changing the position of the outlet).

It is clear that the instability is related here to the inflectional mechanism and that its transient character is specifically due to the strong convection of the perturbation by the base flow as discussed in Cossu & Chomaz (1997) and Chomaz (2005). This is different from the transient energy gain in parallel flows which originates from the tilting of the base-flow vorticity by the perturbations (Schmid 2007). In a global framework, this transient energy gain cannot be captured by considering a single global mode $\hat{q}$ since they are all damped (see figure 2*a*), but may rather be viewed as a result of the cooperation of these damped global modes. From a local point of view, the transient character of the energy gain is interpreted in a different manner. The initial wave packet is amplified while it is travelling in the convectively unstable region, i.e. the shear region of the recirculation bubble, but it decays when it reaches the stable region, i.e. the Poiseuille flow in the downstream part of the channel.

The existence of a three-dimensional mechanism observed for the resonator dynamics (yielding the leading three-dimensional global mode characterized by $k \sim 2$ as seen in §3) and the ability of bounded parallel shear flows to strongly amplify
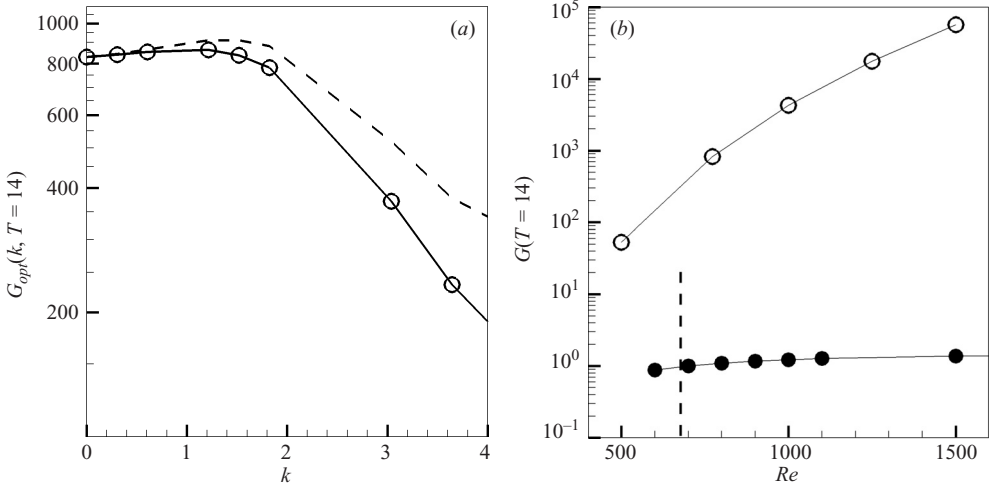
FIGURE 4. (a) Optimal energy gain $G_{opt}(k, T = 14)$ as a function of the transverse wavenumber k for the Reynolds number $Re = 772$ (solid line with circles). For an explanation of the dashed line, see text. (b) Energy gain of the two-dimensional optimal perturbation (open circles) and of the three-dimensional leading global mode (filled circles) over the time $[0, T = 14]$ as a function of the Reynolds number.

the energy of three-dimensional perturbations through a lift-up mechanism (see Schmid & Henningson 2001), suggest a study of the energy gains for $k \neq 0$ in the present recirculation bubble. Preliminary calculations have shown that the optimal time horizon for three-dimensional perturbations is greater than T_{opt}, the optimal time horizon for two-dimensional perturbations. However, the associated energy gain is only slightly different. Therefore we chose to fix the time horizon at $T = T_{opt} = 14$ and to optimize the energy gains for several values of the transverse wavenumber k. The corresponding three-dimensional optimal energy gain $G_{opt}(k, T = 14)$ is depicted as a function of the transverse wavenumber k by a solid line with circles in figure 4(a). For small wavenumbers $k \leqslant 2$, the energy gains achieved by the optimal three-dimensional perturbations are similar to those of the optimal two-dimensional perturbations and even slightly higher for $k \sim 1.5$. For larger wavenumbers $k \geqslant 2$, the optimal energy gain decays abruptly. In order to assess the contribution of viscous diffusion in the transverse direction for increasing k, we depict by a dashed line in figure 4(a) the so-called corrected gain $G'_{opt}(k, T_{opt}) = G_{opt}(k, T_{opt}) \exp[2k^2 T_{opt}/Re]$. This quantity represents the optimal gain when viscous effects are suppressed in the transverse direction, i.e. when the diffusion operator is reduced to $D = Re^{-1}(\partial_x^2 + \partial_y^2)$. We observe that, for $k \geqslant 2$, the corrected gain also decreases, which means that viscous effects in the transverse direction only partly account for the abrupt decrease of $G_{opt}(k, T_{opt})$. Note that viscous effects in the (x, y)-plane are supposed to remain unchanged for increasing k since the corresponding spatial scales of the optimal perturbations in this plane do not vary significantly (not shown here). Consequently viscous effects cannot be invoked to fully explain the abrupt decrease of the energy gain at large k. This decrease may therefore be partly attributed to a loss of coherence in the transverse direction of the perturbations. For quasi-two-dimensional perturbations $k \leqslant 2$ which display a strong transverse coherence, the results show that a small increase in k yields a slightly larger gain, suggesting the existence of a specific

three-dimensional mechanism for the amplifier dynamics. However, this mechanism remains weak compared to the two-dimensional one described previously.

5. Comparison between resonator and amplifier dynamics

In this section, we compare the strength of the resonator and amplifier dynamics. In the linear framework, when the Reynolds number is large enough for the flow to become globally unstable, the leading global mode should emerge for infinitely large times since it is the most amplified global mode. The resonator dynamics, as given by the modal stability analysis in §3, should therefore be observed. The amplifier dynamics, as given by the non-modal analysis in §4, should be irrelevant since it is a transient phenomenon. However flows observed in experiments or numerical simulations are inherently subject to a certain level of external fluctuations, and the amplifier dynamics, which characterizes the transient behaviour of the flow, may become dominant. The strength of the resonator and amplifier dynamics may be compared in the present case to determine if the latter may dominate the former. To that end, we compare for increasing Reynolds numbers the energy gain experienced by the leading three-dimensional global mode during a time interval $[0, T]$ to the energy gain of the optimal two-dimensional initial perturbation over the same time period. Note that the length of the recirculation bubble increases with the Reynolds number and, since the optimal time horizon is approximately the convection time of the wave packet along the recirculation bubble (see the previous section), the optimal time horizon is likely to increase with the Reynolds number. However, the length of the recirculation bubble only slightly increases owing to the confinement induced by the upper wall so that the optimal time horizon only weakly increases with the Reynolds number. Therefore, for all the following calculations, the time horizon has been chosen as $T = 14$, i.e. the optimal time horizon obtained for two-dimensional perturbations at $Re = 772$.

Results are depicted in figure 4(b) where solid symbols show the energy amplification of the leading global mode and open circles the two-dimensional optimal transient energy gain. Starting with the description of the global mode results, we see that, for values of the Reynolds number lower than the critical Reynolds number $Re_c = 695$ (whose position is shown by the vertical dashed line) the energy gain is less than unity, the flow being globally stable, whereas for larger values of the Reynolds number, the energy gain is larger than unity, the flow being globally unstable. However this energy gain is quite moderate even for a Reynolds number two times larger than the critical Reynolds number: for $Re = 1500$, the energy gain during the time period $[0, T = 14]$ is less than 1.5. Focusing now on the non-modal results, the energy gain is less than 10^3 in the subcritical regime but may reach 10^5 for $Re = 1500$. It is striking that for such a moderate Reynolds number the energy of the optimal perturbation may grow by a factor 10^5 in a short time $T = 14$. For comparison, the time for the leading three-dimensional global mode to achieve the same energy growth is much larger, $T = 510$.

In any realistic experiments, external fluctuations are likely to occur during such a large time interval, and, since the time for the flow to amplify these external fluctuations is short, the amplifier dynamics may dominate the resonator dynamics in noisy experiments. To go further, one should address two questions, which are beyond the scope of the present study. The first concerns how the external noise comparatively feeds the optimal initial perturbation and the leading global mode, thus determining their relative initial amplitudes. The second concerns the effect of nonlinearities on

these two dynamics, and the associated saturation of their respective energy growth. This should ultimately determine whether the amplifier or the resonator dynamics is observed in an experiment for a given noise level.

6. Concluding discussion

We first note that no unstable global modes with non-zero frequency have been found in the Reynolds number range considered. Therefore, in a linear framework, only the amplifier dynamics as provided by the optimal perturbation formalism may yield a route to the onset of unsteadiness in the present recirculation flow. From the spatial structure and propagation speed of the most amplified two-dimensional perturbations obtained, we can approximate a frequency that would be measured downstream of the recirculation bubble if the optimal initial perturbation were continuously regenerated. As seen in figure 3(c), the longitudinal wavelength of the vortical structures downstream of the recirculation bubble ($x \sim 8$) is $\lambda_x \sim 1.85 \sim 2h_o$, i.e. two longitudinally aligned counter-rotating vortices which both scale on the height of the downstream channel. As seen previously, these structures propagate at speed $x/t = 0.54$, which is roughly the average speed of the flow $U_o = 0.52$ developing in the downstream channel. The associated frequency would then be $f = U_o/\lambda_x = 0.29$.

Let us briefly give a physical explanation for the fact that $\lambda_x \sim 2h_o$. It is important to note that the amplification of the perturbations stems from the inflectional instability mechanism that exists along the recirculation bubble. The thickness of the shear layer is therefore a key parameter in this selection process. This quantity scales on h_i at the separation point since the inlet profile is a Poiseuille flow in a channel of height h_i. Then it continuously increases along the recirculation bubble and reaches a characteristic value of h_o near the reattachement point. It turns out that this characteristic shear-layer thickness, i.e. h_o, scales with the wavelength of the optimal perturbation λ_x, demonstrating the importance of the rear part of the recirculation bubble in this selection process.

This result may be compared to the one obtained by Kaiktsis *et al.* (1996) in a similar flow, i.e. a Poiseuille flow over a backward-facing step of expansion ratio 1.94. To describe their results, we choose (as in the present study) the step height and the maximum velocity at inlet as reference length and velocity scales. At $Re = 495$, they imposed a low-amplitude monochromatic excitation just upstream of the separation point and explored the time-dependent response of the flow with respect to the excitation frequency f_e. They found that the largest velocity fluctuations were obtained downstream of the recirculation bubble for $f_e = 0.098$. Both frequencies f and f_e, are of the same order of magnitude. Their relative difference is more likely due to differences in the geometry of the two configurations rather than to different mechanisms of frequency selection. Indeed, in both cases, the flow is globally stable and the perturbation growth results from the inflectional instability mechanism in the shear layer of the recirculation bubble. But the overall properties of the flow, i.e. the convection speed in the downstream channel for example, and the properties of the recirculation bubble, for example the recirculation length or the shear layer thickness, are altered by the geometric configuration. In particular, the expansion ratio in the backward-facing step geometry of Kaiktsis *et al.* (1996) ($h_i = 1.06$, $h_o = 2.06$, and $h_o/h_i = 1.94$) is greater than the one in the present geometry ($h_i = 0.723$, $h_o = 0.922$ and $h_o/h_i = 1.28$).

We now show that the frequency f_e obtained in Kaiktsis *et al.* (1996) is analogous to the one obtained in our study, i.e. we show that f_e corresponds roughly to the

frequency of perturbations characterized by a longitudinal wavelength that is twice the height of the downstream channel and which are convected at the average speed of the flow in the downstream channel. This speed is equal to $U_o = 2h_i/(3h_o) = 0.34$ while the wavelength of aligned counter-rotating vortices which scale with the downstream channel height corresponds to $\lambda_x = 2h_o = 4.12$. The associated frequency is then $U_o/\lambda_x = 0.083$ which is close to $f_e = 0.098$. This establishes a close relation between the unsteadiness as observed in Kaiktsis *et al.* (1996) and the present unsteadiness. Also the results in the present article show that the unsteadiness in Kaiktsis *et al.* (1996) is linked to linear optimal perturbations. Note that Kaiktsis *et al.* (1996) performed a local spatial stability analysis at various stations downstream of the step edge to predict the true frequency f_e of the flow. But owing to the thickness of the shear layer (which is related to the choice of a Poiseuille flow at entrance), the assumption of parallelism of the base flow inherent into the local analysis is strongly violated. Therefore, a local stability analysis may only yield a rough idea of the frequency and wavelength of the favoured perturbations. Indeed, Kaiktsis *et al.* (1996) showed that a local analysis yields a whole range of frequencies and wavelengths depending on the choice of the local downstream station where the analysis is applied: for example, structures with frequency 0.16 and wavelength $\lambda_x = 2.8$ should be promoted just downstream of the step edge at $x = 2.1$ (the step edge is located at $x = 0$) while structures with frequency 0.064 and wavelength $\lambda_x = 4.2$ should be favoured for $x \geqslant 15.9$. Hence, a local stability analysis is not able to predict precisely the true frequency $f_e = 0.098$ of the flow (although the order of magnitude is recovered).

The characteristic of our flow configuration as well as of the backward-facing steps studied by Kaiktsis *et al.* (1996) and Barkley *et al.* (2002) is that there is no clear scale separation between the step height, the characteristic thickness of the shear layer and the length of the recirculation bubble. This is due to the Poiseuille flow imposed at the entrance, which exhibits a characteristic thickness of the order of the channel height. As a consequence, the frequency selected by the amplifier dynamics scales with the global spatial scales of the problem, and not solely with the boundary layer thickness at separation, i.e. a local characteristic length scale of the base flow. In that respect, the present recirculation bubble should be distinguished from the separation bubbles induced by an adverse pressure gradient on smooth surfaces studied by Gaster (1966); Pauley, Moin & Reynolds (1990) and Haggmark, Bakchinov & Alfredsson (2000), from the recirculation flow behind a bump in the numerical study of Marquillie & Ehrenstein (2003) and from the backward-facing step flow experimentally investigated by Dovgal & Sorokin (2004). For all these flow configurations, the inflow velocity condition is not a Poiseuille profile but a thin boundary layer profile, and the recirculation bubbles are characterized by a displacement thickness of the boundary layer at separation at least 10 times smaller than the recirculation length. Such a modification of the inflow condition definitely alters the flow dynamics exhibited by the recirculation bubble. For instance, in the experiments by Haggmark *et al.* (2000) and Dovgal & Sorokin (2004), the amplitude spectra measured downstream of the separation bubble show low- and high-frequency oscillations. The high-frequency oscillations are related to the amplification of high-frequency perturbations by the thin shear layer of the recirculation bubble. Haggmark *et al.* (2000) have suggested that the low-frequency oscillations could result from a global instability of the flow, i.e. could be associated with an unstable global mode with non-zero frequency. Marquillie & Ehrenstein (2003) have established a convincing link between low-frequency oscillations and the appearance of an absolutely unstable

region. But, to our knowledge, this low-frequency oscillation has not clearly been associated with a global instability.

The approach developed in the present paper, which consists of examining both the amplifier and resonator dynamics in a global formulation of stability theory, should be performed on recirculation flows exhibiting low- and high-frequency oscillations, i.e. exhibiting a clear scale separation between the thickness of the incoming boundary layer and the overall scales of the geometry. This would help associate the low-frequency oscillations with the resonator dynamics and the high-frequency oscillations to the amplifier dynamics.

REFERENCES

Åkervik, E., Hœpffner, J., Ehrenstein, U. & Henningson, D. S. 2007 Optimal growth, model reduction and control in a separated boundary-layer flow using global modes. *J. Fluid Mech.* **579**, 305–314.

Alving, A. E. & Fernholz, H. H. 1996 Turbulence measurements around a mild separation bubble. *J. Fluid Mech.* **322**, 297–328.

Armaly, B. F., Durst, F., Pereira, J. C. F. & Schonung, B. 1983 Experimental and theoretical investigation of backward-facing step flow. *J. Fluid Mech.* **127**, 473–496.

Barkley, D., Gomes, M. G. M. & Henderson, R. D. 2002 Three-dimensional instability in flow over a backward-facing step. *J. Fluid Mech.* **473**, 167–190.

Beaudoin, J. F., Cadot, O., Aider, J. L. & Wesfreid, J. E. 2004 Three-dimensional stationary flow over a backward-facing step. *Eur. J. Mech.* B/*Fluids* **23**, 147–155.

Boukir, K., Maday, Y., Métivet, B. & Razafindrakoto, E. 1997 A high-order characteristics/finite element method for the incompressible Navier-Stokes equations. *Intl J. Numer. Meth. Fluids* **25**, 1421–1454.

Butler, K. M. & Farrell, B. F. 1992 Three-dimensional optimal perturbations in viscous shear flow. *Phys. Fluids* A **4**, 1637–1650.

Chomaz, J. M. 2005 Global instabilities in spatially developping flows: non-normality and nonlinearity. *Annu. Rev. Fluid Mech.* **37**, 357–392.

Corbett, P. & Bottaro, A. 2001 Optimal linear growth in swept boundary layers. *J. Fluid Mech.* **435**, 1–23.

Cossu, C. & Chomaz, J. M. 1997 Global measures of local convective instabilities. *Phys. Rev. Lett.* **78**, 4387–4390.

Denham, M. K. & Patrick, M. A. 1974 Laminar flow over a downstream-facing step in a two dimensionnal flow channel. *Trans. Inst. Chem. Engrs* **52**, 361–367.

Dovgal, A. V. & Sorokin, A. M. 2004 Interaction of large-scale and small-scale oscillations during separation of a laminar boundary layer. *J. App. Mech. Tech. Phys.* **45**, 517–522.

Ehrenstein, U. & Gallaire, F. 2005 On two-dimensional temporal modes in spatially evolving open flows: the flat-plate boundary layer. *J. Fluid Mech.* **536**, 209–218.

Gallaire, F., Marquillie, M. & Ehrenstein, U. 2007 Three-dimensional transverse instabilities in detached boundary layers. *J. Fluid Mech.* **571**, 221–233.

Gaster, M. 1966 The strcutrue and behaviour of laminar separation bubbles. *AGARD CP-4*, pp. 813–854

Ghia, K. N., Osswald, G. A. & Ghia, U. 1989 Analysis of incompressible massively separated viscous flows using unsteady Navier-Stokes equations. *Intl J. Numer. Meth. Fluids* **9**, 1025–1050.

Haggmark, C. P., Bakchinov, A. A. & Alfredsson, P. H. 2000 Experiments on a two-dimensional laminar separation bubble. *Phil. Trans. R. Soc. Lond.* A **358**, 3193–3205.

Jackson, C. P. 1987 A finite-element study of the onset of vortex shedding in flow past variously shaped bodies. *J. Fluid Mech.* **182**, 23–45.

Kaiktsis, L., Karniadakis, G. E. & Orszag, S. A. 1991 Onset of three-dimensionality, equilibria and early transition in flow over a backward-facing step *J. Fluid Mech.* **231**, 501–528.

Kaiktsis, L., Karniadakis, G. E. & Orszag, S. A. 1996 Unsteadiness and convective instabilities in two-dimensional flow over a backward-facing step *J. Fluid Mech.* **321**, 157–187.

MARQUET, O., LOMBARDI, M., SIPP, D., CHOMAZ, J. M. & JACQUIN, L. 2007 Direct and adjoint global modes of a recirculation bubble: lift-up and convective nonnormalities. *J. Fluid Mech.* (submitted).

MARQUILLIE, M. & EHRENSTEIN, U. 2003 On the onset of nonlinear oscillations in a separating boundary-layer flow. *J. Fluid Mech.* **490**, 169–188.

ORR, W. M. F. 1907 The stability or instability of the steady motions of a perfect liquid and of a viscous liquid. *Proc. R. Irish Acad.* A **27**, 9.

PAULEY, L. L., MOIN, P. & REYNOLDS, W. C. 1990 The structure of two-dimensional separation. *J. Fluid Mech.* **251**, 1–20.

SCHMID, P. J. 2007 Nonmodal stability theory. *Annu. Rev. Fluid Mech.* **39**, 129–162.

SCHMID, P. J. & HENNINGSON, D. S. 2001 *Stability and Transition in Shear Flows*. Springer.

SCHMID, P. J. & HENNINGSON, D. S. 2002 On the stability of a falling liquid curtain. *J. Fluid Mech.* **463**, 163–171.

THEOFILIS, V., HEIN, S. & DALLMANN, U. 2000 On the origins of unsteadiness and three-dimensionality in a laminar separation bubble. *Phil. Trans. R. Soc. Lond.* A **358**, 3229–3246.

TREFETHEN, L. N., TREFETHEN, A. E., REDDY, S. C. & DRISCOLL, T. A. 1993 Hydrodynamic stability without eigenvalues. *Science* **261**, 578–584.

WILLIAMS, P. T. & BAKER, A. J. 1997 Numerical simulations of laminar flow over a three-dimensional backwad-facing step. *Intl J. Numer. Meth. Fluids* **24**, 1159–1183.

ZEBIB, A. 1987 Stability of viscous flow past a circular cylinder. *J. Engng Maths* **21**, 155–165.